American Mineralogist, Volume 100, pages 1533–1543, 2015

Silica polymorphs in lunar granite: Implications for granite petrogenesis on the Moon

STEPHEN M. SEDDIO[1,]*, RANDY L. KOROTEV[1], BRADLEY L. JOLLIFF[1] AND ALIAN WANG[1]

[1]Department of Earth and Planetary Sciences and McDonnell Center for the Space Sciences, Washington University, St. Louis, Missouri 63130, U.S.A.

ABSTRACT

Granitic lunar samples largely consist of granophyric intergrowths of silica and K-feldspar. The identification of the silica polymorph present in the granophyre can clarify the petrogenesis of the lunar granites. The presence of tridymite or cristobalite would indicate rapid crystallization at high temperature. Quartz would indicate crystallization at low temperature or perhaps intrusive, slow crystallization, allowing for the orderly transformation from high-temperature silica polymorphs (tridymite or cristobalite). We identify the silica polymorphs present in four granitic lunar samples from the Apollo 12 regolith using laser Raman spectroscopy. Typically, lunar silica occurs with a hackle fracture pattern. We did an initial density calculation on the hackle fracture pattern of quartz and determined that the volume of quartz and fracture space is consistent with a molar volume contraction from tridymite or cristobalite, both of which are less dense than quartz. Moreover, we analyzed the silica in the granitic fragments from Apollo 12 by electron-probe microanalysis and found it contains up to 0.7 wt% TiO_2, consistent with initial formation as the high-temperature silica polymorphs, which have more open crystal structures that can more readily accommodate cations other than Si. The silica in Apollo 12 granitic samples crystallized rapidly as tridymite or cristobalite, consistent with extrusive volcanism. The silica then inverted to quartz at a later time, causing it to contract and fracture. A hackle fracture pattern is common in silica occurring in extrusive lunar lithologies (e.g., mare basalt). The extrusive nature of these granitic samples makes them excellent candidates to be similar to the rocks that compose positive relief silicic features such as the Gruithuisen Domes.

Keywords: Silica, polymorph identification, granite, Moon, granophyre, volcanism, Raman spectroscopy

INTRODUCTION

Among the Apollo samples and lunar meteorites, lunar granitic samples, also referred to as "felsite," are rare. In this paper, we use the adjective "granitic" to describe lithologies, monomict or polymict, with a component of granophyric intergrowth of K-feldspar and silica beyond blebs formed by silicate liquid immiscibility in the mesostasis of basalts. We reserve the term "granite" for igneous lithologies that mostly consist of granophyre with accessory minerals that have compositions consistent with extreme fractional crystallization (fayalite, hedenbergite). Only 22 lunar samples have been identified to be granitic, accounting for less than 100 g total mass (Seddio et al. 2013), <0.03% of the mass of all Apollo samples. Compared to terrestrial rocks, silica minerals are rare in lunar samples and most commonly occur as accessory concentrations of cristobalite or tridymite in mare basalts (Smith and Steele 1976; Lucey et al. 2006). Silica has been identified in basalts from all Apollo sites. Silica also has been identified in gabbro (e.g., Sippel 1971), microgabbro (Smith et al. 1970; Klein et al. 1971), monzogabbro (e.g., Jolliff 1991), ferroan anorthosite (Stewart et al. 1972), and granite (e.g., Seddio et al. 2013, 2014). The low-pressure silica polymorphs, quartz, tridymite, and cristobalite, have been widely reported in lunar samples, but the high-pressure silica polymorphs (coesite or stishovite) have been reported only rarely (Ohtani et al. 2011). The near absence of coesite and stishovite is unexpected because these polymorphs are typically present in impact-related rocks on Earth, and most of the lunar surface is saturated with craters. Papike et al. (1997) suggested that absence of high-pressure silica polymorphs in lunar samples may result from the paucity of silica minerals in the target rocks and the impact-induced volatilization of silica in the lunar surface environment.

Soon after the first Apollo samples were brought to Earth, Dence et al. (1970) and others noted that the silica in the Apollo samples tended to exhibit a fracture pattern, which has been described as "curved fractures" and as having a "cracked appearance" (Smith et al. 1970), or as having a "crinkled texture" (Neal et al. 1994). In this work, we describe the fracture pattern of silica as a "hackle" fracture pattern (Fig. 1). Fracturing within lunar silica has been used to distinguish the polymorph as cristobalite (e.g., Ryder 1976; Jolliff 1991) and as "relict cristobalite" (Jolliff et al. 1999). The latter identification assumes that the silica originally crystallized as cristobalite and later underwent a molar volume contraction to quartz. Fracturing in a silica phase has been used to identify which polymorph is present; however, because the silica polymorph in a sample indicates the pressure and temperature conditions under which the sample crystallized, it is important to determine the identity of a silica polymorph using an analytical method, such as laser Raman spectroscopy or laser Raman imaging, that can directly, and in situ, identify the

---

* E-mail: sseddio@levee.wustl.edu

0003-004X/15/0007–1533$05.00/DOI: http://dx.doi.org/10.2138/am-2015-5058

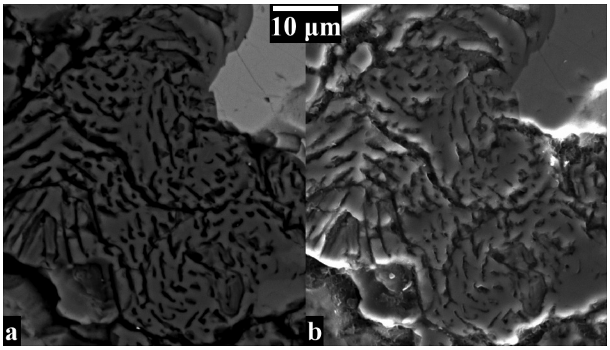

FIGURE 1. (**a**) Backscattered electron (BSE) image and (**b**) secondary electron (SE) image of quartz with a hackle fracture pattern in 12023,147-10.

structural form of a SiO_2 polymorph. The laser Raman spectra of quartz, tridymite, and cristobalite are readily distinguishable from each other (Downs 2006; Ling et al. 2011).

The identification of the silica polymorph present in the granophyre can clarify the petrogenesis of the lunar granites. Robinson and Taylor (2011) noted that if lunar granite crystallized at depth (~10 km; Holmberg and Rutherford 1994), where the conditions might have been favorable for silicate-liquid immiscibility, and slow cooling may have allowed for density separation of the complementary felsic and mafic liquids, the silica phase crystallizing from the felsic liquid should have cooled slowly enough for quartz to form. Alternatively, if silicic lava were to erupt at the lunar surface (i.e., at very low pressure), the silica should occur as a high-temperature polymorph (tridymite, 870–1470 °C, or cristobalite, 1470–1705 °C; Holleman and Wiberg 1984; Rykart 1995; Wenk and Bulakh 2003).

A variety of techniques have been used to distinguish or identify the silica polymorphs present within lunar samples, including optical petrography (e.g., Dence et al. 1970; Frondel et al. 1970; Dollase et al. 1971; Sippel 1971; Quick et al. 1981; Warren et al. 1983; Marvin et al. 1991), electron diffraction (Champness et al. 1971), X-ray diffraction (e.g., Dence et al. 1970; Frondel et al. 1970; Appleman et al. 1971; Dollase et al. 1971; Champness et al. 1971), and laser Raman spectroscopy (Jolliff et al. 1999; Robinson and Taylor 2011; Seddio et al. 2013, 2014). Sippel and Spencer (1970) and Sippel (1971) identified and distinguished between silica polymorphs; however, it is unclear whether the polymorphs were identified using optical petrography or cathodoluminescence petrography. From a survey of the literature, the silica polymorphs in 23 granitic samples have been identified or distinguished by various means. Quick et al. (1981) identified quartz and tridymite in granitic breccia 12013 using optical methods. Marvin et al. (1991) also used optical methods to distinguish quartz in "potash rhyolite" 12070,102-5. Robinson and Taylor (2011) identified quartz as the silica polymorph in 19 granitic lunar samples using laser Raman spectroscopy. Seddio et al. (2013) and Seddio et al. (2014) identified quartz as the silica polymorph that occurs in granitic fragments 12032,366-19 and 12023,147-10, respectively, using laser Raman spectroscopy. Here, we identify the silica polymorphs present in four additional, recently characterized Apollo 12 granitic fragments using laser Raman spectroscopy imaging, and we interpret the laser Raman spectroscopy data in conjunction with the textures of the analyzed silica polymorphs and trace concentrations of non-Si cations in the analyzed silica grains.

EXPERIMENTAL METHODS

Samples 12001,909-14, 12032,367-16, 12033,634-30, and 12033,634-34 are granitic lithic fragments from the 2–4 mm grain-size fraction of the Apollo 12 regolith allocated for the studies of Barra et al. (2006) and Korotev et al. (2011) along with 354 other lithic fragments. We examined all 358 fragments under a binocular microscope and analyzed each one individually for concentrations of 26 chemical elements by INAA (instrumental neutron activation analysis; Korotev et al. 2011), including eight REEs (La, Ce, Nd, Sm, Eu, Tb, Yb, and Lu). Eight fragments were found to be granitic in composition (high K, low Fe, high Th, and high U), with 12023,147-10 (Seddio et al. 2014) being the smallest at 2.67 mg.

We identified the silica polymorphs that occur in Apollo 12 granitic fragments 12001,909-14, 12032,367-16, 12033,634-30, and 12033,634-34 by laser Raman spectroscopy analysis using an inVia Raman System (Renishaw) at Washington University. We obtained laser Raman spectroscopy data using both spot analysis mode and Streamline imaging mode (i.e., dynamic line-scanning Raman mapping; Bernard et al. 2008). The 532 nm line of a diode-pumped solid-state laser was used as the excitation source. Analyses were done using a 50× long-working-distance objective (NA = 0.5), which condenses the laser beam into a spot of 1 µm diameter on the sample in spot analysis mode or into an elliptical spot of 1 × 30 µm for the dynamic line-scanning Raman mapping mode. The objective also collects backscattered Raman photons from the sample, which are sent to a Raman spectrometer through a width-adjustable slit. A 2400 line/mm holographic grating disperses the collected Raman photons into a Raman Stokes-shift range of 50 to 1300 cm^{-1} for this study, with a spectral resolution of ~1 cm^{-1}. Additional details of our laser Raman spectroscopy analysis methodology can be found in Wang et al. (2014).

We analyzed silica polymorphs for Na, Mg, Al, Si, P, K, Ti, Cr, and Fe by quantitative wavelength-dispersive spectroscopy electron-probe microanalysis (EPMA) using the JEOL 8200 electron microprobe at Washington University. EPMA was done on sample 12023,147-10 (sample petrography and mineralogy described in Seddio et al. 2014) in addition to the four samples that were analyzed by laser Raman spectroscopy in this study. Analyses were done using a 15 kV accelerating voltage and a 25 nA beam current. Na, Mg, Al, Si, P, K, Ca, Ti, Cr, and Fe were counted on peak ($K\alpha$) for 52.5, 20, 35, 35, 30, 30, 30, 40, 20, and 30 s, respectively (results and uncertainties in Table 1). Silica in sample 12032,367-16 has the highest TiO_2 concentration among our silica-bearing lunar granitic samples. Many of the analysis spots in 12032,367-16 are within 100 µm of an ilmenite grain, the Ti (and Fe) of which could be fluoresced by Bremsstrahlung X-rays generated by the electron probe interacting with silica (e.g., Wark and Watson 2006). However, because the TiO_2 concentration is not correlated with distance from the ilmenite grain, we are confident that the TiO_2 in the analyses is representative of the SiO_2 phase in sample 12032,367-16.

To investigate whether the hackle fracture pattern (e.g., Fig. 1) present in some silica occurrences formed by a molar volume contraction caused by a lower density polymorph (tridymite or cristobalite) changing to a higher density polymorph (quartz), we used secondary electron (SE) images to calculate fracture area and silica area (A_{Frac} and A_{Qtz}, respectively). We assume that the fracture and silica areas in the images are representative of the fracture and silica volumes (V_{Frac} and V_{Qtz}, respectively). The density of the higher temperature polymorph—the silica polymorph that originally crystallized—can be calculated using the following method:

$$\rho_{HighT} = \rho_{Qtz}\frac{V_{Qtz}}{V_{HighT}} \cong \rho_{Qtz}\frac{A_{Qtz}}{A_{HighT}} = \rho_{Qtz}\frac{A_{Qtz}}{A_{Qtz} + A_{Frac}}$$

which we refer to hereafter as the initial density calculation. We used backscattered electron (BSE) images to confirm the location of boundaries between silica and other phases. Images were made using an accelerating voltage of 15 kV and a probe current of 1 nA to minimize spot size. In addition to the aforementioned granitic lunar samples, we used the initial density calculation to calculate the initial density of the quartz exhibiting a hackle fracture pattern in Apollo 12 granite fragment 12032,366-19 (characterized in Seddio et al. 2013).

We determined modal abundances for four granitic fragments. Phase abundances were determined using image analysis of BSE mosaics and X-ray maps to essentially count all pixels of each phase, which we then divided by the total number of pixels (background subtracted) to obtain the area fraction, which we take to be proportional to the volume fraction. Based on counting statistics, the error associated with the modal abundances of major and accessory phases is typically <1%; the error associated with the modal abundances of trace phases is typically <30%. The error associated with trace phases is high because, in the BSE images and X-ray maps, these phases are represented by as few as 12 pixels each (the total sample areas are represented by millions of pixels).

Sample 12001,909-14

Sample 12001,909-14 is a 7.01 mg complex polymict granitic breccia (Fig. 2). We describe the petrography of sample 12001,909-14 in terms of seven areas (Fig. 3) on the basis of textures and mineral compositions. The modal abundances of the phases within the seven areas are in Table 2. The ranges of end-member compositions and average compositions for the major minerals in Areas 1 and 2, Areas 3 and 4, Areas 5 and 6, and Area 7 are in Tables 3, 4, 5, and 6, respectively. Individual analyses for the major minerals in all areas of sample 12001,909-14 are in Appendix 1[1]. Area

TABLE 1. Quantitative analyses of silica phases in granitic fragments from Apollo 12

Sample	12001,		12001,		12023,		12032,		12033,		12033,	
Fragment	909-14		909-14		147-10		367-16		634-30		634-34	
Phase	Quartz		Amorphous silica		Quartz		Cristobalite		Quartz		Quartz	
	wt%	σ	wt%	σ	wt%	σ	wt%	σ	wt%	σ	wt%	σ
SiO_2	99.6	1.55	98.4	1.49	99.3	1.27	95.5	3.59	97.9	0.41	97.2	1.58
TiO_2	0.15	0.06	0.20	0.02	0.10	0.02	0.49	0.13	0.16	0.06	0.11	0.06
Al_2O_3	0.41	0.26	1.38	0.99	0.24	0.23	2.17	0.82	0.92	0.28	1.16	1.27
Cr_2O_3	<0.02	–	<0.02	–	<0.02	–	<0.02	–	<0.02	–	<0.02	–
FeO	0.13	0.05	0.04	0.02	0.07	0.03	0.50	0.31	0.09	0.07	0.09	0.03
MgO	<0.01	–	<0.01	–	<0.01	–	<0.04	–	<0.01	–	<0.01	–
CaO	0.08	0.09	0.15	0.13	0.09	0.09	0.57	1.10	0.07	0.01	0.22	0.24
Na_2O	<0.02	–	0.14	0.09	<0.02	–	0.17	0.17	0.07	0.02	0.07	0.08
K_2O	0.06	0.07	0.40	0.59	0.03	0.02	0.33	0.34	0.28	0.20	0.27	0.38
P_2O_5	<0.02	0.04	<0.02	0.01	<0.02	0.02	0.21	0.30	<0.02	0.02	<0.01	0.01
Sum	100.4		100.7		99.8		99.9		99.5		99.1	

Note: "σ" is one standard deviation.

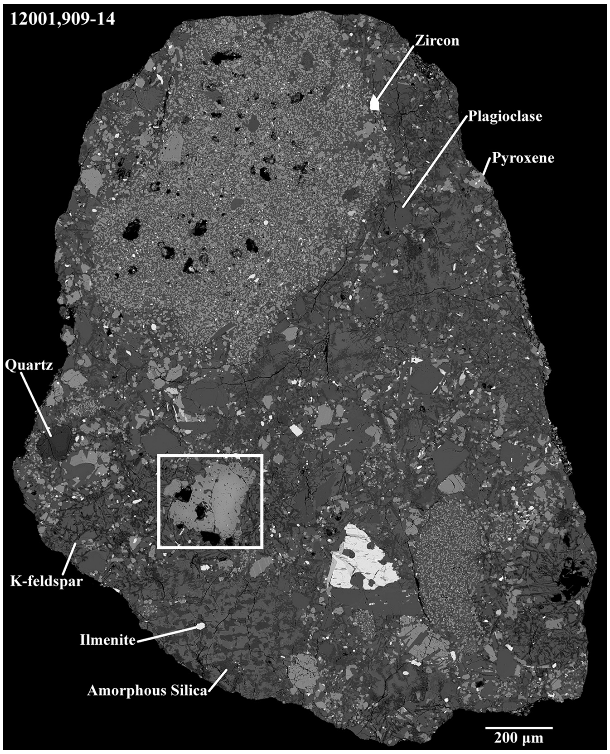

FIGURE 2. BSE image of 12001,909-14. In order of brightness from darkest to brightest, minerals (or phases) are quartz, amorphous silica, plagioclase, K-feldspar, high-Ca pyroxene, low-Ca pyroxene, ilmenite, and zircon. Zirconolite and monazite also occur but the grains are too small to resolve in this image. The white rectangle highlights the zoned 0.15 × 0.2 mm high-Ca pyroxene grain (core: $En_{\sim10}Wo_{\sim41}Fs_{\sim49}$, rim: $En_{\sim34}Wo_{\sim39}Fs_{\sim27}$). See Figure 4 for a high-resolution BSE image, X-ray maps, and a laser Raman image of the zoned pyroxene grain.

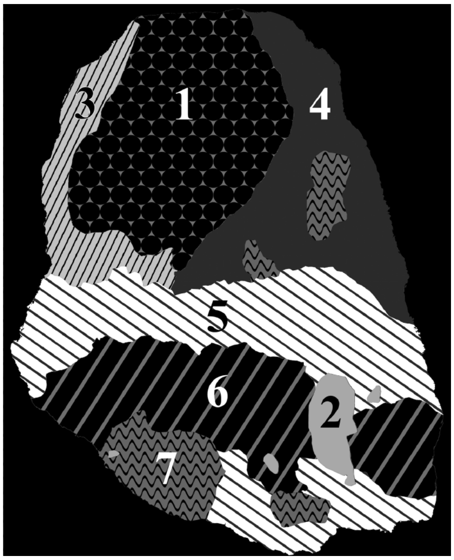

FIGURE 3. Locations of seven areas in sample 12001,909-14 that were identified based on petrographic similarities.

TABLE 2. Modal abundances of 12001,909-14 areas

Area	1	2	3	4	5	6	7
Silica	4.8	4.5	23	34	22	27	37
K-feldspar	13	29.5	27	29	15	24	46
Plagioclase	37	34	30	26	41	30	15
High-Ca pyroxene	16	11	5.3	3.4	8.0	10	Trace
Low-Ca pyroxene	27	19	13	5.0	9.5	3.6	0.8
Ilmenite	1.1	2.0	1.0	0.5	0.9	3.8	0.4
Ca-Phos.	1.1	–	0.4	0.3	2.4	1.1	–
Zircon	Trace	–	Trace	1.2	0.1	Trace	Trace
Zirconolite	–	–	–	–	Trace	–	–
Monazite	–	–	–	–	–	–	Trace

Notes: All values are in vol%. "Ca-Phos." refers to apatite and/or RE-merrillite. "–" means that the phase is not present in the area. Areas are depicted in Figure 3.

---

[1] Deposit item AM-15-75058, Appendices. Deposit items are free to all readers and found on the MSA web site, via the specific issue's Table of Contents (go to http://www.minsocam.org/MSA/AmMin/TOC/).

TABLE 3. Average compositions of major minerals in Areas 1 and 2 of sample 12001,909-14

	Area 1								Area 2							
Phase	Kfs		Pl		High-Ca Px		Low-Ca Px		Kfs		Pl		High-Ca Px		Low-Ca Px	
End-member composition	$An_{1.1–15}Ab_{12–19}Or_{65–86}Cn_{1.2–1.5}$		$An_{50–84}Ab_{15–48}Or_{0.4–1.8}Cn_{<0.09}$		$En_{34–37}Fs_{28–39}Wo_{23–38}$		$En_{40–42}Fs_{49–53}Wo_{6.3–9.7}$		$An_{3.7–26}Ab_{12–24}Or_{49–83}Cn_{0.9–1.8}$		$An_{38–86}Ab_{13–49}Or_{0.3–17}Cn_{<0.2}$		$En_{\sim34}Fs_{\sim27}Wo_{\sim39}$		$En_{42–43}Fs_{50–51}Wo_{5.9–7.9}$	
N	17		22		2		6		7		5		1		5	
	wt%	σ	wt%	σ	wt%	σ	wt%	σ	wt%	σ	wt%	σ	wt%	σ	wt%	σ
SiO_2	64.9	1.58	51.8	2.44	51.8	0.57	51.0	0.38	62.0	1.41	51.1	4.67	51.1	–	51.2	0.95
TiO_2	0.08	0.03	0.05	0.02	0.71	0.08	0.37	0.04	0.10	0.06	0.08	0.04	0.79	–	0.39	0.13
Al_2O_3	20.2	1.35	31.3	1.93	0.95	0.17	0.61	0.58	20.6	2.25	31.9	4.11	1.80	–	0.54	0.15
Cr_2O_3	n.a.	–	n.a.	–	0.34	0.02	0.20	0.03	n.a.	–	n.a.	–	0.41	–	0.20	0.02
FeO	0.45	0.05	0.66	0.23	20.3	4.6	30.4	0.84	0.84	0.66	0.47	0.15	16.0	–	30.1	0.48
MnO	<0.03	–	<0.03	–	0.33	0.01	0.45	0.02	<0.03	–	<0.03	–	0.24	–	0.44	0.03
MgO	<0.01	–	0.07	0.11	12.1	0.64	13.8	0.24	0.31	0.41	0.06	0.05	11.5	–	14.3	0.18
CaO	1.49	1.38	13.8	1.95	14.6	5.02	3.71	0.56	4.04	3.00	13.4	5.42	18.0	–	3.16	0.37
BaO	0.75	0.08	<0.06	–	n.a.	–	n.a.	–	0.60	0.28	0.32	0.22	n.a.	–	n.a.	–
Na_2O	1.77	0.38	3.53	1.02	0.09	0.03	<0.02	–	2.48	1.45	2.60	1.63	0.21	–	0.05	0.03
K_2O	13.1	1.75	0.15	0.08	n.a.	–	<0.01	–	9.77	4.53	1.77	3.66	n.a.	–	0.05	0.04
P_2O_5	n.a.	–	n.a.	–	<0.03	–	<0.04	–	n.a.	–	n.a.	–	0.06	–	0.17	0.18
Sum	102.7	–	101.4	–	101.2	–	100.5	–	100.7	–	101.7	–	100.1	–	100.6	–

Notes: Areas 1 and 2 refer to the areas shown in Figure 3. "N" refers to the number of analyses averaged. "Kfs" refers to K-feldspar. "Pl" refers to plagioclase. "Px" refers to pyroxene. "Cn" refers to celsian—the Ba-feldspar end-member. "n.a." means "not analyzed."

TABLE 4. Average compositions of major minerals in Areas 3 and 4 of sample 12001,909-14

	Area 3								Area 4							
	Kfs		Pl		High-Ca Px		Low-Ca Px		Kfs		Pl		High-Ca Px		Low-Ca Px	
	$An_{2.7–14}Ab_{17–21}Or_{63–78}Cn_{2.4–3.0}$		$An_{68–87}Ab_{13–31}Or_{0.4–1.2}Cn_{<0.1}$		$En_{\sim33}Fs_{\sim28}Wo_{\sim39}$		$En_{\sim41}Fs_{\sim51}Wo_{\sim7.7}$		$An_{6.7–11}Ab_{19–21}Or_{66–71}Cn_{2.0–2.7}$		$An_{64–89}Ab_{10–34}Or_{0.5–1.3}Cn_{<0.1}$		$En_{\sim32}Fs_{\sim28}Wo_{\sim40}$		$En_{\sim41}Fs_{51–52}Wo_{7.7–8.7}$	
N	3		5		1		1		2		5		1		2	
	wt%	σ	wt%	σ	wt%	σ	wt%	σ	wt%	σ	wt%	σ	wt%	σ	wt%	σ
SiO_2	63.1	1.07	49.2	1.68	50.7	–	50.1	–	63.5	1.34	49.4	2.67	50.9	–	49.9	0.28
TiO_2	0.09	0.02	0.08	0.03	0.86	–	0.46	–	0.07	0.07	0.06	0.03	0.83	–	0.36	0.01
Al_2O_3	20.7	1.10	33.3	1.32	1.03	–	0.41	–	20.7	0.28	32.8	2.00	0.84	–	0.36	0.01
Cr_2O_3	n.a.	–	n.a.	–	0.37	–	0.15	–	<0.04	–	<0.04	–	0.28	–	0.18	0.02
FeO	0.18	0.03	0.41	0.07	17.1	–	30.9	–	0.15	0.06	0.30	0.03	16.7	–	30	0.14
MnO	<0.04	–	<0.02	–	0.29	–	0.48	–	<0.05	–	<0.06	–	0.25	–	0.43	0.02
MgO	<0.01	–	<0.03	–	11.1	–	13.6	–	<0.01	–	0.03	0.02	10.9	–	13.5	0.21
CaO	1.73	1.12	15.8	1.36	18.2	–	3.58	–	1.79	0.59	15.5	2.04	18.7	–	3.77	0.4
BaO	1.45	0.18	<0.06	–	<0.09	–	<0.08	–	1.32	0.30	<0.08	–	<0.08	–	<0.08	–
Na_2O	2.24	0.31	2.40	0.71	0.09	–	<0.03	–	2.28	0.16	2.65	1.15	0.14	–	0.03	0.01
K_2O	12.0	1.32	0.13	0.06	0.04	–	<0.01	–	11.8	0.64	0.14	0.06	0.07	–	0.05	0.04
P_2O_5	n.a.	–	n.a.	–	<0.05	–	<0.05	–	<0.03	–	0.05	0.01	<0.04	–	<0.04	–
Sum	101.5	–	101.3	–	99.8	–	99.7	–	101.6	–	100.9	–	99.6	–	98.6	–

Notes: Areas 3 and 4 refer to the areas shown in Figure 3. "N" refers to the number of analyses averaged. "Kfs" refers to K-feldspar. "Pl" refers to plagioclase. "Cn" refers to celsian—the Ba-feldspar end-member. "Px" refers to pyroxene. "n.a." means "not analyzed."

TABLE 5. Average compositions of major minerals in Areas 5 and 6 of sample 12001,909-14

	Area 5								Area 6							
	Kfs		Pl		High-Ca Px		Low-Ca Px		Kfs		Pl		High-Ca Px		Low-Ca Px	
	$An_{6.0–13}Ab_{16–20}Or_{65–76}Cn_{2.0–2.3}$		$An_{47–87}Ab_{12–48}Or_{0.2–5.1}Cn_{<0.1}$		$En_{33–36}Fs_{26–34}Wo_{33–39}$		$En_{39–43}Fs_{47–52}Wo_{7.2–12}$		$An_{1.2–31}Ab_{11–22}Or_{53–84}Cn_{1.2–4.0}$		$An_{56–89}Ab_{11–42}Or_{0.1–1.8}Cn_{<0.1}$		$En_{10–35}Fs_{27–49}Wo_{37–42}$		$En_{40–43}Fs_{47–54}Wo_{5.3–13}$	
N	3		15		8		11		12		21		52		6	
	wt%	σ	wt%	σ	wt%	σ	wt%	σ	wt%	σ	wt%	σ	wt%	σ	wt%	σ
SiO_2	64.0	0.97	49.0	2.62	51.3	0.95	50.7	0.86	63.6	2.21	49.0	2.43	49.9	1.34	51.1	0.97
TiO_2	0.11	0.02	0.05	0.02	0.79	0.22	0.46	0.15	0.13	0.12	0.21	0.15	0.85	0.10	0.41	0.12
Al_2O_3	20.8	0.72	33.6	2.12	1.12	0.44	0.59	0.24	20.3	1.36	33.4	1.84	0.90	0.14	0.81	0.99
Cr_2O_3	n.a.	–	n.a.	–	0.38	0.10	0.23	0.08	n.a.	–	n.a.	–	0.21	0.13	0.17	0.05
FeO	0.29	0.04	0.26	0.10	17.0	1.48	29.5	1.25	0.23	0.17	0.34	0.15	20.9	4.20	29.7	1.6
MnO	<0.03	–	<0.03	–	0.26	0.03	0.44	0.03	<0.03	–	<0.04	–	0.29	0.05	0.45	0.05
MgO	<0.01	–	0.03	0.01	11.6	0.32	13.9	0.38	0.10	0.10	0.03	0.01	8.07	2.97	13.7	0.73
CaO	1.87	0.68	16.2	2.14	17.6	1.50	4.21	0.68	1.62	1.82	16.0	1.83	18.5	0.43	3.38	1.36
BaO	1.19	0.07	<0.06	–	n.a.	–	n.a.	–	1.39	0.53	0.07	0.01	n.a.	–	n.a.	–
Na_2O	2.03	0.19	2.24	1.07	0.12	0.01	0.05	0.04	1.82	0.34	2.34	0.98	0.10	0.02	<0.02	–
K_2O	12.1	0.90	0.14	0.20	n.a.	–	<0.01	–	12.6	1.77	0.11	0.07	0.08	0.12	n.a.	–
P_2O_5	n.a.	–	n.a.	–	0.03	0.02	<0.02	–	n.a.	–	n.a.	–	0.03	0.02	0.03	0.02
Sum	102.4	–	101.5	–	100.2	–	100.1	–	101.8	–	101.5	–	99.8	–	99.8	–

Notes: Areas 5 and 6 refer to the areas shown in Figure 3. "N" refers to the number of analyses averaged. "Kfs" refers to K-feldspar. "Pl" refers to plagioclase. "Px" refers to pyroxene. "Cn" refers to celsian—the Ba-feldspar end-member. "n.a." means "not analyzed."

1 is a 1 × 0.75 mm rounded clast of basaltic impact melt and accounts for 23% of the section. Area 2 accounts for 2.4% of sample 12001,909-14 and comprises four rounded basaltic impact melt clasts, the largest of which is 0.2 × 0.4 mm. The most distinct difference between Areas 1 and 2 is that Area 2 contains more K-feldspar. Area 3 accounts for 6.6% of the section and comprises mineral fragments in a granophyre matrix. Area 4, 15% of the sample, is similar to Area 3 but contains less pyroxene. Area 5 accounts for 26% of the sample, and Area 6 represents 19%. Most of the high-Ca pyroxene in Area 6 occurs as a 0.15 × 0.2 mm zoned grain (core: $En_{\sim10}Wo_{\sim41}Fs_{\sim49}$, rim: $En_{\sim34}Wo_{\sim39}Fs_{\sim27}$; Figs. 2 and 4). Area 7 accounts for 8% of sample 12001,909-14. A trace amount of high-Ca pyroxene is present in Area 7, as

TABLE 6. Average compositions of major minerals in Area 7 of sample 12001,909-14

	Kfs		Pl		Low-Ca Px	
	$An_{0.8–13}Ab_{13–18}$ $Or_{53–84}Cn_{3.1–5.1}$		$An_{43–46}Ab_{51–53}$ $Or_{1.9–5.7}Cn_{<0.3}$		$En_{\sim39}Fs_{\sim53}$ $Wo_{\sim7.6}$	
N	10		4		1	
	wt%	σ	wt%	σ	wt%	σ
SiO_2	64.5	1.06	58.4	0.74	50.3	–
TiO_2	0.06	0.02	0.04	0.01	0.35	–
Al_2O_3	19.9	0.62	27.2	0.21	0.39	–
Cr_2O_3	n.a.	–	n.a.	–	0.17	–
FeO	0.05	0.02	0.16	0.02	30.9	–
MnO	<0.03	–	<0.03	–	0.49	–
MgO	<0.01	–	0.04	0.02	13.0	–
CaO	0.63	0.71	9.20	0.21	3.49	–
BaO	2.30	0.34	0.11	0.06	<0.09	–
Na_2O	1.69	0.23	5.89	0.03	<0.03	–
K_2O	13.4	0.79	0.58	0.31	0.07	–
P_2O_5	n.a.	–	n.a.	–	<0.05	–
Sum	102.5	–	101.6	–	99.2	–

Notes: Area 7 refers to the area shown in Figure 3. "N" refers to the number of analyses averaged. "Kfs" refers to K-feldspar. "Pl" refers to plagioclase. "Px" refers to pyroxene. "Cn" refers to celsian—the Ba-feldspar end-member. "n.a." means "not analyzed."

fine (~1 μm) exsolution lamellae in the low-Ca pyroxene. We are unable to analyze the exsolution lamellae of high-Ca pyroxene without sampling the adjacent low-Ca pyroxene, but we presume that the composition of the Area 7 high-Ca pyroxene is similar ($En_{32–37}Wo_{\sim39}Fs_{26–43}$) to that in the rest of sample 12001,909-14 (except the large zoned high-Ca pyroxene in Area 6) because the high- and low-Ca pyroxene compositions are homogenous throughout the sample.

The granophyre in Area 7 is different from that found in the rest of the sample. The Area 7 silica is not fractured, whereas the silica in the other areas exhibits a hackle fracture pattern (e.g., Fig. 5). The intergrowths of K-feldspar and silica in Area 7 are approximately twice as wide as the intergrowths in the other areas. Additionally, the K-feldspar in Area 7 has the highest Cn content ("Cn" refers to celsian—the Ba-feldspar end-member) in the sample (as high as $Cn_{5.1}$); whereas Area 6 K-feldspar has $Cn_{<4}$, and the rest of the K-feldspar in sample 12001,909-14 has $Cn_{<3}$.

Sample 12032,367-16

Sample 12032,367-16 is a 7.80 mg friable, strongly fractured granitic breccia consisting of 41.8% plagioclase, 24.3% silica, 18.7% low-Ca pyroxene, 14.1% K-feldspar, 0.6% apatite, 0.3% ilmenite, and 0.2% zircon with trace amounts of zirconolite. The ranges of end-member compositions and average compositions for the major minerals in sample 12032,367-16 are in Table 7. Individual analyses of the major minerals in sample 12032,367-16 are in Appendix 2[1]. In the portions of the sample where the granophyre occurs, it consists of K-feldspar intergrown with fracture-free silica occurring in the interstices between blocky plagioclase grains (Fig. 6 inset).

Sample 12033,634-30

Sample 12033,634-30 is a 7.50 mg monomict granitic breccia (Fig. 7) consisting of 31.3% plagioclase, 20.6% silica with a hackle fracture pattern, 18.4% high-Ca pyroxene, 16.5% K-feldspar, 8.3% low-Ca pyroxene, 2.0% RE-merrillite, 1.5% apatite, 1.1% ilmenite, 0.2% zircon, and trace amounts of olivine (one grain) and troilite (two grains). The ranges of end-member compositions and average compositions for the major minerals in sample 12033,634-30 are in Table 8. Individual analyses of the major minerals in sample 12033,634-30 are in Appendix 3[1]. The sample is composed of angular and sub-rounded mineral fragments in a granophyric matrix of K-feldspar and silica. One corner of the section (right corner of the fragment in Fig. 7) contains a significantly higher proportion of granophyre compared to the rest of the sample. This area also contains the only occurrence of fayalitic olivine. The largest pyroxene grain is intergrown with apatite.

Sample 12033,634-34

Sample 12033,634-34 is a 6.96 mg granite (Fig. 8) comprising 30.3% ternary feldspar, 24.0% silica, 21.1% K-feldspar, 8.7% pyroxene, 7.1% fayalitic olivine, 4.0% apatite, 3.9% RE-merrillite, 1.0% ilmenite, and trace amounts of plagioclase, zirconolite, zircon, and baddeleyite. The ranges of end-member compositions and average compositions for the major minerals in sample 12033,634-34 are in

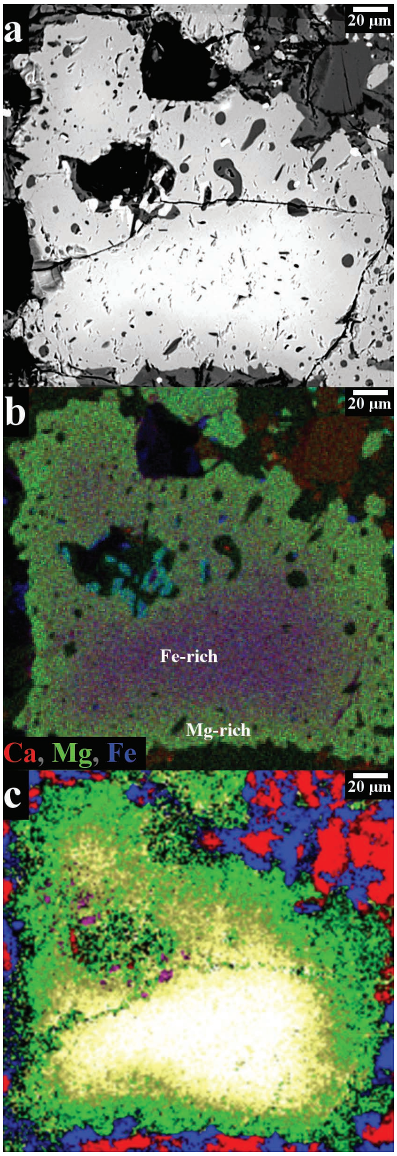

FIGURE 4. Images of the zoned high-Ca pyroxene grain in Area 6 of 12001,909-14. The core has a composition of $En_{10}Wo_{41}Fs_{49}$; the rim has a composition of $En_{34}Wo_{39}Fs_{27}$. (**a**) Backscattered electron image in which zoning is evidenced by brighter core and darker rim. (**b**) Ca, Mg, and Fe X-ray maps merged into an RGB image. The purple core indicates hedenbergite, and the yellow-green rim is the more magnesian high-Ca pyroxene. Teal is low-Ca pyroxene—a reaction product of fayalite with surrounding quartz and the magnesian lithology. Fayalite occurs with quartz and K-feldspar in an inclusion that crystallized from late-stage melt. Inclusions of fayalite+K-feldspar+quartz also occur in hedenbergite in lunar granite 12032,366-19 (Seddio et al. 2013). Blue specks are ilmenite. Teardrop-shaped inclusion is K+Si glass surrounding Ca-phosphate (red speck). (**c**) Laser Raman image in which white, yellow, and green represent pyroxene: white-yellow tones represent areas with spectra most like hedenbergite; green-gray tones represent areas with spectra most like diopside. Red areas have spectra that match K-feldspar. Blue areas have spectra matching quartz. Magenta areas have spectra matching orthopyroxene (low-Ca pyroxene in "X-ray"). Black areas have spectra with no Raman peaks (holes or fractures) or spectra that do not match pyroxene, quartz, or K-feldspar. (Color online.)

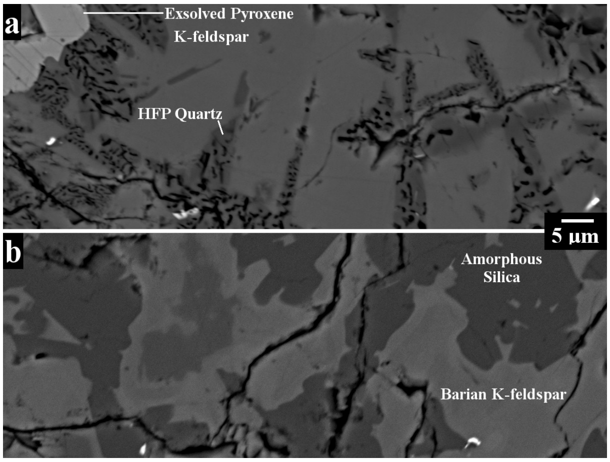

FIGURE 5. BSE images of typical occurrences of quartz with a hackle fracture pattern (**a**) and amorphous silica (**b**) in sample 12001,909-14. The K-feldspar in **b** is noticeably brighter in contrast compared to the K-feldspar (**a**) owing to its higher Ba content. The brightest phase in **a** is zirconolite; the brightest phase in **b** is monazite.

TABLE 7. Average compositions of major minerals in sample 12032,367-16

	Kfs		Pl		Low-Ca Px	
	An$_{4.0–8.8}$Ab$_{18–21}$ Or$_{65–72}$Cn$_{5.0–5.6}$		An$_{80–88}$Ab$_{11–18}$ Or$_{0.2–5.8}$Cn$_{<0.3}$		En$_{52–59}$Fs$_{31–38}$ Wo$_{3.5–17}$	
N	2		8		6	
	wt%	σ	wt%	σ	wt%	σ
SiO_2	63.8	0.78	46.8	1.31	52.9	0.57
TiO_2	0.14	0.01	0.07	0.02	0.51	0.11
Al_2O_3	20.9	1.63	34.4	0.58	0.59	0.16
Cr_2O_3	<0.05	–	n.a.	–	0.25	0.05
FeO	0.13	0.01	0.22	0.10	22.4	1.59
MnO	<0.05	–	<0.03	–	0.33	0.02
MgO	<0.02	–	0.03	0.02	19.4	0.99
CaO	1.18	0.54	17.2	0.58	4.15	2.29
BaO	2.73	0.42	<0.08	–	<0.08	–
Na_2O	2.01	0.01	1.64	0.29	0.03	0.02
K_2O	10.8	1.56	0.22	0.32	<0.01	–
P_2O_5	<0.05	–	<0.04	–	<0.05	–
Nb_2O_5	n.a.	–	n.a.	–	n.a.	–
Sum	101.7	–	100.6	–	100.6	–

Notes: "N" refers to the number of analyses averaged. "Kfs" refers to K-feldspar. "Pl" refers to plagioclase. "Px" refers to pyroxene. "Cn" refers to celsian—the Ba-feldspar end-member. "n.a." means "not analyzed."

Table 9. Individual analyses of the major minerals in sample 12033,634-34 are in Appendix 4[1]. Some grains of fayalite, K-feldspar, ternary feldspar, and, quartz are large enough to be visible with the unaided eye and are all irregularly shaped. The large fayalite grain in Figure 8 is strongly fractured. Three silica grains are >0.1 mm and have curved boundaries. Pyroxene is typically zoned and elongate with parallel fractures oriented perpendicular to the direction of grain elongation. The remainder of sample 12033,634-34 consists primarily of granophyric intergrowths of silica and K-feldspar, the grains of which are in some cases <1 mm in maximum dimension.

RESULTS

Using laser Raman spectroscopy, we identified quartz in samples 12001,909-14, 12033,634-30, and 12033,634-34; cristobalite in sample 12032,367-16; and amorphous silica in sample 12001,909-14. Examples of Raman spectra from quartz-bearing samples are shown in Figure 9, and peak positions used to identify phases are listed in Table 10. Figures 10 and 11 show examples of Raman spectra from a cristobalite-bearing sample and the amorphous SiO_2-bearing sample, respectively. In sample

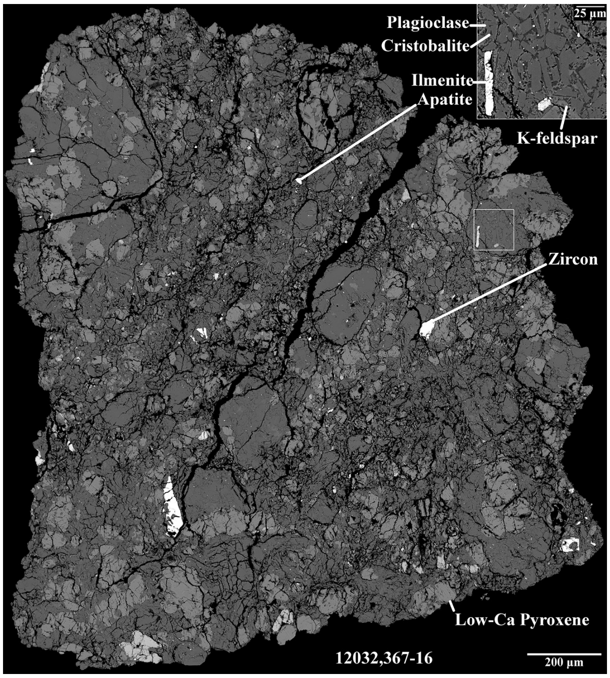

FIGURE 6. BSE image mosaic of 12032,367-16 with high-resolution BSE image inset (white rectangle). In order of brightness from darkest to brightest, minerals are cristobalite, plagioclase, K-feldspar, low-Ca pyroxene, apatite, ilmenite, and zircon. Zirconolite is the brightest phase but is only visible as bright specks in the inset image.

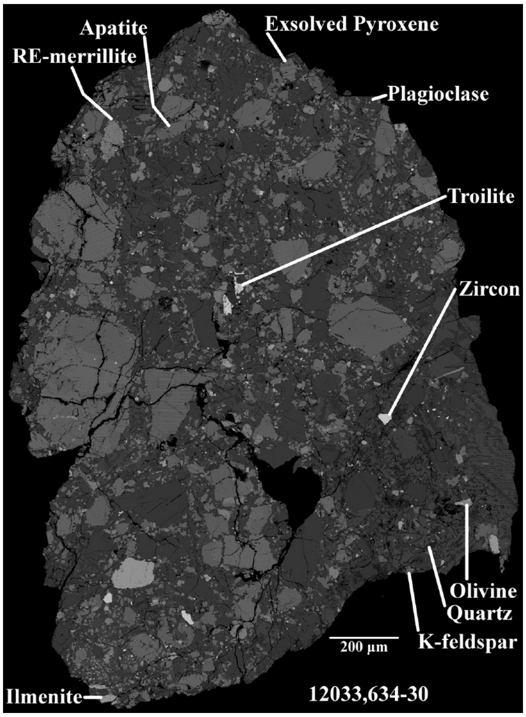

FIGURE 7. BSE image mosaic of 12033,634-30. In order of brightness from darkest to brightest, minerals (or phases) are quartz, plagioclase, K-feldspar, high-Ca pyroxene, low-Ca pyroxene, apatite, RE-merrillite, olivine, ilmenite, zircon, and troilite.

TABLE 8. Average compositions of major minerals in sample 12033,634-30

	Kfs		Pl		High-Ca Px		Low-Ca Px		Ol		Ilm	
	$An_{0.7–14}Ab_{13–32}$ $Or_{52–83}Cn_{2.3–4.9}$		$An_{44–65}Ab_{34–53}$ $Or_{0.8–3.0}Cn_{<0.2}$		$En_{25–29}Fs_{33–38}$ $Wo_{36–39}$		$En_{30–32}Fs_{60–63}$ $Wo_{5.7–10}$		$Mg'_{2.9–4.2}$		$Fo_{20–22}$	
N	17		22		2		6		6		5	
	wt%	σ	wt%	σ	wt%	σ	wt%	σ	wt%	σ	wt%	σ
SiO_2	63.1	1.23	54.4	2.12	50.5	1.16	49.8	0.68	31.7	0.3	<0.02	–
TiO_2	0.07	0.02	0.05	0.02	0.95	0.5	0.48	0.21	0.28	0.03	52.6	0.92
Al_2O_3	19.9	0.93	29.2	1.39	0.75	0.2	0.28	0.1	<0.02	–	<0.02	–
Cr_2O_3	n.a.	–	n.a.	–	0.05	0.01	0.03	0.01	<0.02	–	0.08	0.03
FeO	0.18	0.12	0.27	0.1	22.5	1.65	34.7	1.88	59.0	0.26	44.9	0.24
MnO	<0.03	–	<0.03	–	0.34	0.05	0.54	0.05	0.58	0.03	0.42	0.04
MgO	<0.01	–	<0.01	–	8.96	0.51	10.1	0.56	8.89	0.27	1.04	0.09
CaO	0.96	0.91	11.4	1.57	16.5	1.76	4.89	2.25	0.05	0.01	0.06	0.03
BaO	1.81	0.38	<0.06	–	n.a.	–	n.a.	–	n.a.	–	n.a.	–
Na_2O	2.05	0.62	4.92	0.85	0.1	0.02	0.04	0.01	<0.03	–	<0.03	–
K_2O	12.7	1.63	0.21	0.08	<0.01	–	<0.01	–	0.03	0.01	n.a.	–
P_2O_5	n.a.	–	n.a.	–	n.a.	–	n.a.	–	n.a.	–	n.a.	–
Nb_2O_5	n.a.	–	n.a.	–	n.a.	–	n.a.	–	n.a.	–	0.68	0.4
Sum	100.8	–	100.5	–	100.7	–	100.9	–	100.5	–	99.8	–

Notes: "N" refers to the number of analyses averaged. "Kfs" refers to K-feldspar. "Pl" refers to plagioclase. "Px" refers to pyroxene. "Ol" refers to olivine. "Ilm" refers to ilmenite. "Cn" refers to celsian—the Ba-feldspar end-member. "n.a." means "not analyzed."

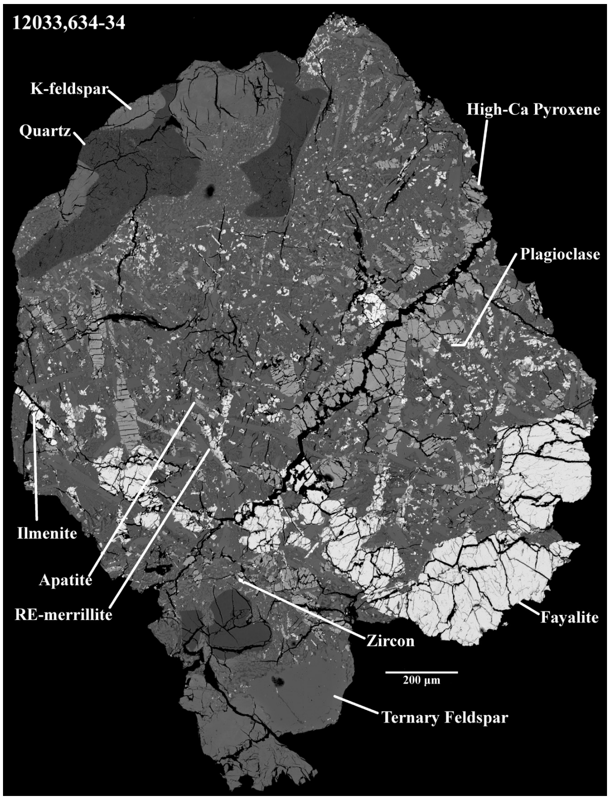

FIGURE 8. BSE image mosaic of 12033,634-34. In order of brightness from darkest to brightest, minerals (or phases) are quartz, plagioclase, ternary feldspar, K-feldspar, high-Ca pyroxene, apatite, RE-merrillite, fayalite, ilmenite, and zircon. Zirconolite and baddeleyite are the brightest phases and occur as elongate grains and specks, respectively.

12001,909-14, Areas 3, 4, 5, and 6 contain quartz, all of which have a hackle fracture pattern; however, Area 7 contains amorphous silica that does not have a hackle fracture pattern. Sample 12032,367-16 contains cristobalite without a hackle fracture pattern. Samples 12023,147-10, 12033,634-30, and 12033,634-33 contain quartz with a hackle fracture pattern.

Because, compared to quartz, the relatively more open crystal structures of tridymite and cristobalite can better accommodate cations other than Si (Papike and Cameron 1976; Smith and Steele 1984), the measurement of trace or minor concentrations of other cations can aid with the identification of the silica polymorph present. The results of the EPMA for minor elements (Ti, Al, Cr, Fe, Mg, Ca, Na, K, and P) in silica of lunar granite are summarized in Table 11 and Figure 12. Because the silica grains in the lunar granitic samples of this study are typically only a few micrometers wide, most of the Na_2O, Al_2O_3, K_2O, and CaO present in the analyses are attributable to overlap of the electron probe interaction volume with adjacent feldspar (yielding Na, Al, K, and Ca) or the secondary fluorescence from characteristic Si X-rays (yielding Na and Al).

The results of the initial density calculation of the quartz with a hackle fracture pattern are summarized in Table 11. The initial silica densities that we calculate from quartz (density: 2.65 g/cm^3; Will et al. 1988) with a hackle fracture pattern in the six (including samples 12023,147-10 and 12032,366-19) granitic lunar samples that we have studied are similar to the densities of the high-temperature, low-pressure silica polymorphs (tridymite, density: 2.18–2.28 g/cm^3; Kihara 1978; and cristobalite, density: 2.32–2.36 g/cm^3; Schmahl et al. 1992). The initial silica densities are most consistent with tridymite, except in sample 12033,634-34, which has an initial density calculation most like that of cristobalite.

DISCUSSION

In lunar granitic lithologies, the silica polymorphs quartz, cristobalite, and tridymite, as well as amorphous silica, have been identified (Quick et al. 1981; Robinson and Taylor 2011; Seddio et al. 2013). Typically, quartz is the silica polymorph intergrown with K-feldspar or plagioclase in lunar granite. In granitic lunar samples, all silica that has been identified as quartz using laser Raman spectroscopy has a hackle fracture pattern. Moreover, all silica with a hackle fracture pattern in the samples that we have studied has been found definitively to be quartz. In granitic lunar samples, cristobalite and amorphous silica have not been observed to occur with the distinctive hackle fracture pattern. Tridymite has only been reported in granitic breccia

TABLE 9. Average compositions of major minerals in sample 12033,634-34

	Kfs $An_{2.2–18}Ab_{12–28}$ $Or_{51–80}Cn_{2.3–8.0}$		Tfs $An_{28–52}Ab_{23–29}$ $Or_{25–41}Cn_{<0.1–4.9}$		Pl $An_{49–51}Ab_{47–49}$ $Or_{1.1–1.7}Cn_{<0.2}$		High-Ca Px $En_{16–20}Fs_{40–43}$ $Wo_{40–41}$		Ol $Fo_{9.0–13}$		Ilm $Mg'_{0.8–1.1}$	
N	15		26		2		6		6		5	
	wt%	σ	wt%	σ	wt%	σ	wt%	σ	wt%	σ	wt%	σ
SiO_2	63.3	1.01	55.5	2.28	54.0	1.56	48.9	0.42	30.9	0.32	<0.02	–
TiO_2	0.05	0.02	0.04	0.02	0.05	0.02	1.27	0.08	0.14	0.10	51.8	0.27
Al_2O_3	19.2	0.75	25.6	1.38	27.5	0.68	1.38	0.18	<0.02	–	<0.02	–
Cr_2O_3	n.a.	–	n.a.	–	n.a.	–	0.03	0.01	<0.02	–	<0.02	–
FeO	0.58	0.35	1.56	1.92	0.79	0.09	24.3	0.69	64.8	1.20	46.2	0.80
MnO	0.03	0.00	0.08	0.04	<0.04	–	0.35	0.02	0.76	0.08	0.39	0.01
MgO	<0.02	–	<0.02	–	<0.03	–	5.76	0.44	4.27	0.62	0.25	0.03
CaO	1.48	0.89	7.92	1.55	10.3	0.32	18.3	0.12	0.20	0.08	0.06	0.01
BaO	2.46	0.66	0.87	0.79	0.09	0.03	n.a.	–	n.a.	–	n.a.	–
Na_2O	1.85	0.47	2.60	0.31	5.50	0.16	0.10	0.02	<0.03	–	<0.03	–
K_2O	10.6	1.68	4.63	0.44	0.25	0.07	<0.02	–	<0.02	–	n.a.	–
P_2O_5	n.a.	–	n.a.	–	n.a.	–	n.a.	–	n.a.	–	<0.02	–
Nb_2O_5	n.a.	–	n.a.	–	n.a.	–	n.a.	–	n.a.	–	0.53[a]	0.04[a]
Sum	99.6	–	98.8	–	98.5	–	100.3	–	101.1	–	99.2	–

[a] Nb_2O_5 was measured for only two of the analyses. "N" refers to the number of analyses averaged. "Kfs" refers to K-feldspar. "Tfs" refers to ternary feldspar. "Pl" refers to plagioclase. "Px" refers to pyroxene. "Ol" refers to olivine. "Ilm" refers to ilmenite. "Cn" refers to celsian—the Ba-feldspar end-member. "n.a." means "not analyzed."

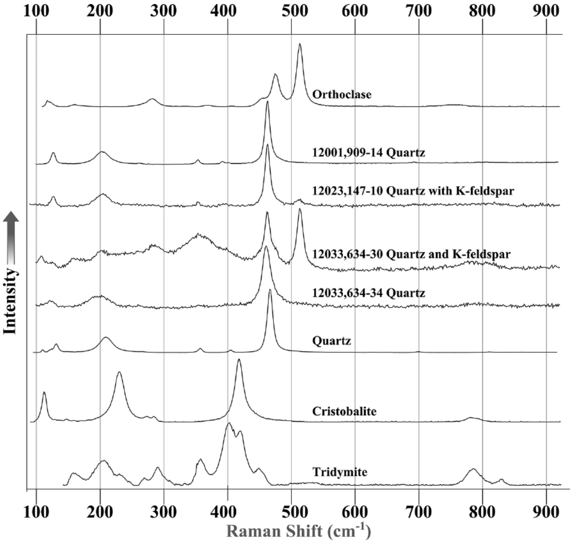

FIGURE 9. Laser Raman spectra of quartz identified in samples 12001,909-14, 12023,147-10 (Seddio et al. 2014), 12033,634-30, and 12033,634-34. K-feldspar peaks are present in quartz spectra obtained from samples 12023,147-10 and 12033,634-30. We include quartz, orthoclase (K-feldspar), cristobalite, and tridymite standard spectra from the RRUFF database (Downs 2006) for comparison with our analyses.

TABLE 10. Raman peak positions for identified phases

Sample	Phase	Peaks used for identification (cm^{-1})	
12001,909-14	Quartz	463	353
	K-feldspar	512	472
12023,147-10	Quartz	463	–
	K-feldspar	513	–
12032,637-16	Cristobalite	415	229
	Plagioclase	508	481
12033,634-30	Quartz	462	–
	K-feldspar	513	476
12033,634-34	Quartz	460	–
Reference spectra	Quartz	464	358
	Cristobalite	418	230
	K-feldspar	513	474
	Plagioclase (oligoclase)	508	480

Notes: We include quartz, orthoclase (K-feldspar), and cristobalite standard spectra from the RRUFF database (Downs 2006; Ling et al. 2011) for comparison with our analyses.

12013 (optically identified by Quick et al. 1981). Appendix 5[1] contains a survey of all lunar samples that contain silica and what polymorphs have been identified therein.

The fractured nature of lunar silica has been interpreted to result from a molar volume inversion. Dence et al. (1970) and Smith et al. (1970) attributed fractures in cristobalite—identified optically and by X-ray diffraction—to an inversion from high to low cristobalite. However, because quartz is the silica polymorph typically found in granitic lunar samples, we attribute the hackle fracture pattern of quartz in granitic lunar samples to a molar volume inversion from cristobalite (density: 2.32–2.36 g/cm^3; Schmahl et al. 1992) or tridymite (density: 2.18–2.28 g/cm^3; Kihara 1978) to quartz (density: 2.65 g/cm^3; Will et al. 1988) on the basis of the initial density calculation. Inverting from a lower to a higher density phase would produce isotropic tensional stress within the quartz, causing it to fracture (i.e., the hackle pattern). This process of fracturing is similar, but greater in magnitude, to that fracturing that can occur with the transition of β- to α-cristobalite (e.g., Carpenter et al. 1998; Damby et al. 2014).

Inversion of tridymite or cristobalite to quartz is a reconstructive phase transition (e.g., Lakshtanov et al. 2007), requiring reconfiguration of Si–O bonds. Although this inversion might be constrained (as opposed to a displacive transformation), we think that transformation of a high-temperature silica polymorph to quartz is the best explanation for the hackle fracture patterns observed in the quartz of granitic lunar samples. Perhaps this transformation was aided by impact-induced heating events experienced by granitic samples resulting in their excavation and possibly other impact events during their >3 Ga history.

The Raman spectra collected from lunar quartz all have peaks that are shifted to lower positions from the typical quartz peak positions (Table 10; Fig. 9). This red shift is a result of stress within the SiO_2 structural framework and has been attributed to shock metamorphism (McMillan et al. 1992; Ling et al. 2011). A result of the experiments of McMillan et al. (1992) is that the major peak position of unshocked quartz (464 cm^{-1}) is shifted down to 455 cm^{-1} after shock to a peak pressure of 31.4 GPa.

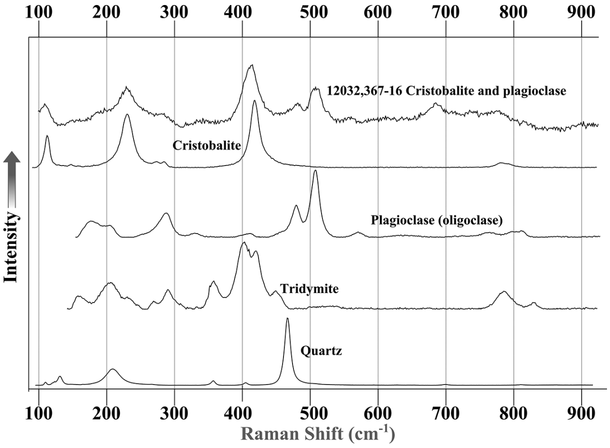

FIGURE 10. Laser Raman spectrum of cristobalite identified in sample 12032,367-16 that also contains a contribution from nearby plagioclase. We include cristobalite, plagioclase (oligoclase), tridymite, and quartz standard spectra from the RRUFF database (Downs 2006) for comparison with our analyses.

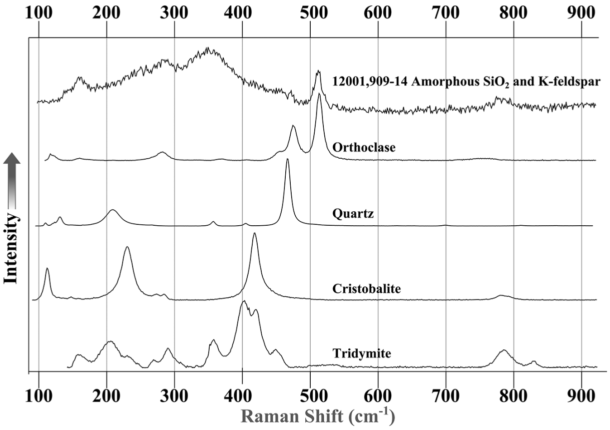

FIGURE 11. Laser Raman spectrum of amorphous silica identified in sample 12001,909-14 that also contains a contribution from nearby K-feldspar. We include orthoclase (K-feldspar), quartz, cristobalite, and tridymite standard spectra from the RRUFF database (Downs 2006) for comparison with our analyses.

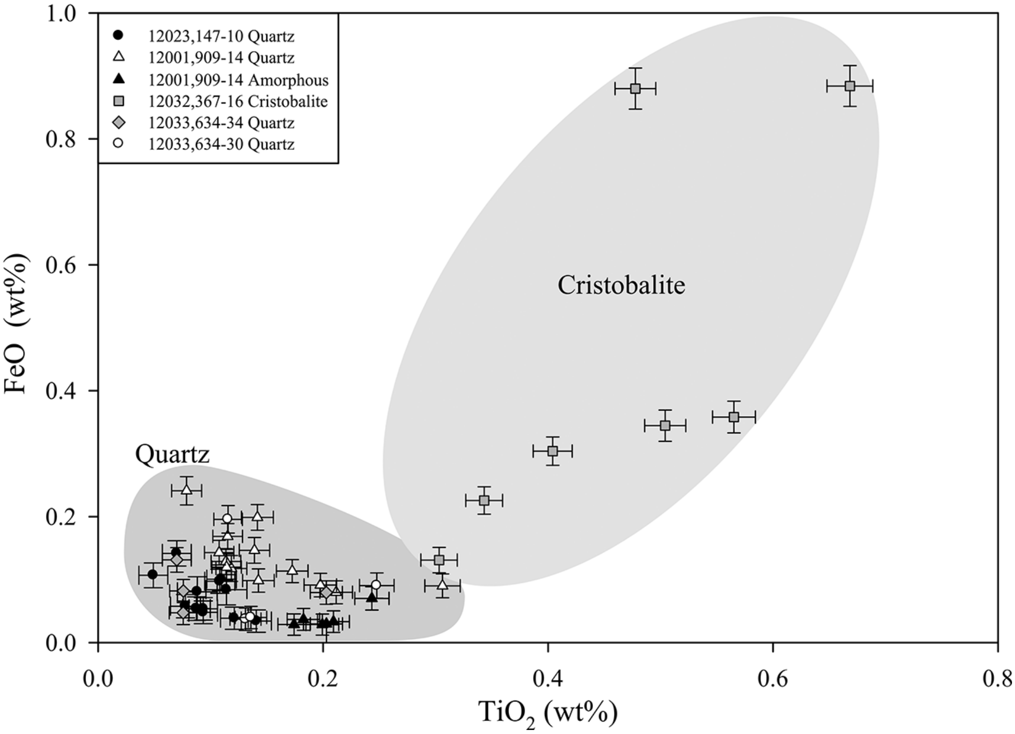

FIGURE 12. Concentrations of FeO and TiO$_2$ measured in silica by EPMA. Error bars represent the "% error" calculated from counting statistics.

Additionally, the magnitude of the peak shift in the quartz Raman spectrum is directly, but not linearly, related to the magnitude of shock pressure experienced by a sample (McMillan et al. 1992). Based on this relationship, the granites in this study, which exhibit a maximum peak shift down to 460 cm^{-1} (sample 12033,634-34; Table 10) from unshocked quartz (464 cm^{-1}), should not have experienced shock pressures greater than ~25 GPa. An alternative explanation of the peak shift of the Raman spectra of quartz in this study is that the fracturing of the quartz after inversion from a phase of higher density did not perfectly relieve the stress within the silica. Perhaps this remnant stress may be responsible for the observed shift of the peaks in the Raman spectra of quartz with a hackle fracture pattern.

Compared to quartz, tridymite and cristobalite can incorporate greater amounts of cations other than Si—typically, Na, Al, K, Ti, and Fe (Fig. 12)—into their relatively open crystal

TABLE 11. Initial density calculation

Sample	12001,	12023,	12032,	12033,	12033,
Fragment	909-14	147-10	366-19	634-30	634-34
Phase	Quartz	Quartz	Quartz	Quartz	Quartz
ρ_q	2.65	2.65	2.65	2.65	2.65
ρ_i	2.21	2.17	2.18	2.23	2.43
σ	0.01	0.02	0.05	–	0.04
$\rho_{trid.}$	2.18–2.28				
$\rho_{crist.}$	2.32–2.36				

Notes: Results of the initial density calculation (see text) for quartz with a hackle fracture pattern. "ρ_q" refers to the assumed density of quartz used in the calculation. "ρ_i" refers to the calculated initial density for the silica in each sample and is an average of calculated initial densities from multiple secondary electron images for all samples except for 12033,634-30, from which only one high-resolution secondary electron image was taken. "σ" is one standard deviation of the initial densities calculated from multiple secondary electron images of each sample. Densities of tridymite (Kihara 1978) and cristobalite (Schmahl et al. 1992) are given for comparison. All values are in g/cm^3.

structures (Papike and Cameron 1976; Smith and Steele 1984). In tridymite and cristobalite, Si substitution typically involves Al^{3+} replacing Si^{4+} with charge balance maintained by the introduction of Na^+ or K^+ into interstitial vacancies (Papike and Cameron 1976). Smith and Steele (1984) reported Na, Al, K, and Ti abundances in samples of terrestrial quartz, tridymite, and cristobalite samples (5, 4, and 1 samples, respectively). Because our Na, Al, and K data likely include a contribution from neighboring feldspars, we are only confident comparing our Ti data to the data of Smith and Steele (1984), who reported 0.06–0.22 wt% TiO_2 in tridymite, and <0.01 wt% TiO_2 in quartz. In the lunar granitic samples containing quartz and amorphous silica, TiO_2 concentrations are within the range of concentrations that Smith and Steele (1984) report for tridymite. However, the cristobalite we identified in sample 12032,367-16 contains 0.30–0.67 wt% TiO_2 (Fig. 12).

The occurrence of quartz as the silica polymorph in lunar granite has been interpreted to mean that quartz-bearing lunar granite crystallized at depth (Robinson and Taylor 2011). If crystallization occurred at a depth where the pressure was sufficiently high, the parent magma could have crystallized quartz. Alternatively, if crystallization occurred at depth but at pressures low enough and temperatures high enough for the primary crystallization of tridymite or cristobalite, perhaps slow cooling may have permitted orderly transformations from high-temperature polymorphs to quartz. However, in those lunar granite samples that contain quartz with a hackle fracture pattern, it is more likely that the melts crystallized rapidly at high temperature, with primary crystallization and preservation of tridymite or cristobalite as the silica polymorph until a structural inversion occurred at some later time, causing a reduction in molar volume. The petrographic evidence for the crystallization of silica as a high-temperature polymorph—tridymite or cristobalite—is supported by high TiO_2 concentrations. Furthermore, the small (<1 mm) grain sizes that typically occur in lunar granites indicate rapid crystallization, in comparison to other lunar primary igneous rocks that exhibit coarser grain sizes. Sample 15405,12 is an exception, with grain sizes >1 mm, silica with a hackle fracture pattern, and is interpreted to have crystallized in a pluton (Ryder 1976). In sample 12033,634-34, some grain sizes are >1 mm, but irregular grain sizes and ternary feldspar are indicative of rapid crystallization.

IMPLICATIONS

The silica polymorph contained in lunar granite is most commonly quartz. These quartz grains typically exhibit a hackle fracture pattern indicating that they inverted from a high-temperature, low-pressure polymorph, either tridymite or cristobalite. The preservation of high-temperature silica polymorphs, before a molar volume contraction to quartz at some point later, and the fine-grained textures of most granitic lunar samples indicate that that the samples experienced relatively rapid cooling (e.g., rhyolitic volcanism). Laser Raman spectroscopy is very sensitive to the differences in structure and symmetry of the silica polymorphs and is thus a well-suited method to identify, unambiguously and in situ, the silica polymorph(s) present in granitic lunar samples. The laser Raman spectra, coupled with textural and compositional data, provide a clear indication of the crystallization of the silica polymorphs and a firm constraint on crystallization conditions.

The Apollo 12 granitic samples of this study contain silica that we identified using laser Raman spectroscopy to be cristobalite, amorphous silica, or quartz with a hackle fracture pattern. The EPMA measurements of the silica in the Apollo 12 granitic samples are consistent with analyses of high-temperature silica polymorphs. The initial density calculations of quartz with a hackle fracture pattern in Apollo 12 granites indicate that the silica crystallized as a high-temperature polymorph. We conclude that the Apollo 12 granitic samples must have crystallized at a temperature above 870 °C and that they did so rapidly enough to preserve the high-temperature polymorph. The fine-grained nature of the granitic samples also indicates rapid crystallization. Rapid crystallization from high temperature suggests that the Apollo 12 granitic samples are a product of extrusive magmatism.

Granitic lunar samples are silicic and have the highest Th concentrations among known lunar lithologies (e.g., Seddio et al. 2013). Some locations on the Moon are also known to be silicic based on orbital radiometry (Glotch et al. 2010) and rich in Th based on orbital γ-ray spectroscopy (e.g., Lawrence et al. 2003; Hagerty et al. 2006; Jolliff et al. 2011), such as the Gruithuisen Domes and the Mairan Domes. This compositional similarity has led to the interpretation that granitic lunar samples might represent volcanic exposures similar to these domes.

ACKNOWLEDGMENTS

This work was funded by NASA grant NNX11AJ66G (R.L.K.) and NASA MFRP grant NNX10AM89G (A.W.). We thank Allan Treiman, Marc Freis, and Associate Editor Steven Simon for their insightful reviews that improved this paper. Additionally, we thank Axel Wittmann for helpful comments.

REFERENCES CITED

Appleman, D.E., Nissen, H.-U., Stewart, D.B., Clark, J.R., Dowty, E., and Huebner, J.S. (1971) Studies of lunar plagioclase, tridymite, and cristobalite. Proceedings of the 2nd Lunar Science Conference, 1, 117–133.

Barra, F., Swindle, T.D., Korotev, R.L., Jolliff, B.L., Zeigler, R.A., and Olson, E. (2006) ^{40}Ar-^{39}Ar dating on Apollo 12 regolith: Implications on the age of Co-pernicus and the source of non-mare materials. Geochimica et Cosmochimica Acta, 70, 6016–6031.

Bernard, S., Beyssac, O., and Benzerara, K. (2008) Raman mapping using advanced line-scanning systems: Geological applications. Applied Spectroscopy, 62, 1180–1188.

Carpenter, M.A., Salje, E.K.H., and Graeme-Barber, A. (1998) Spontaneous strain as a determinant of thermodynamic properties for phase transitions in minerals. European Journal of Mineralogy, 10, 621–691.

Champness, P.E., Dunham, A.C., Gibb, F.G.F., Giles, H.N., MacKenzie, W.S., Stumpfl, E.F., and Zussman, J. (1971) Mineralogy and petrology of some

Apollo 12 lunar samples. Proceedings of the 2nd Lunar Science Conference, 1, 359–376.

Damby, D.E., Llewellin, E.W., Horwell, C.J., Williamson, B.J., Najorka, J., Cressey, G., and Carpenter, M. (2014) The α–β phase transition in volcanic cristobalite. Journal of Applied Crystallography, 47, 1205–1215.

Dence, M.R., Douglas, J.A.V., Plant, A.G., and Traill, R.J. (1970) Petrology, mineralogy and deformation of Apollo 11 samples. Proceedings of the Apollo 11 Lunar Science Conference, 1, 315–340.

Dollase, W.A., Cliff, R.A., and Wetherill, G.W. (1971) Note on tridymite in rock 12021. Proceedings of the 2nd Lunar Science Conference, 1, 141–142.

Downs, R.T. (2006) The RRUFF Project: an integrated study of the chemistry, crystallography, Raman and infrared spectroscopy of minerals. Program and Abstracts of the 19th General Meeting of the International Mineralogical Association in Kobe, Japan, O03-13.

Frondel, C., Klein, C. Jr., Ito, J., and Drake, J.C. (1970) Mineralogical and chemical studies of Apollo 11 lunar fines and selected rocks. Proceedings of the Apollo 11 Lunar Science Conference, 1, 445–474.

Glotch, T.D., Lucey, P.G., Bandfield, J.L., Greenhagen, B.T., Thomas, I.R., Elphic, R.C., Bowles, N., Wyatt, M.B., Allen, C.C., Hanna, K.D., and Paige, D.A. (2010) Highly silicic compositions on the Moon. Science, 329, 1510.

Hagerty, J.J., Lawrence, D.J., Hawke, B.R., Vaniman, D.T., Elphic, R.C., and Feldman, W.C. (2006) Refined thorium abundances for lunar red spots: Implications for evolved, nonmare volcanism on the Moon. Journal of Geophysical Research, 111, E06002.

Holleman, A.F., and Wiberg, E. (1984) Lehrbuch Der Anorganischen Chemie. Walter Gruyter Verlag, New York.

Holmberg, B., and Rutherford, M.J. (1994) An experimental study of KREEP basalt evolution. Abstracts of the 25th Lunar and Planetary Science Conference, 557.

Jolliff, B.L. (1991) Fragments of quartz monzodiorite and felsite in Apollo 14 soil particles. Proceedings of Lunar and Planetary Science Conferences, 21, 101–118.

Jolliff, B.L., Floss, C., McCallum, I.S., and Schwartz, J.M. (1999) Geochemistry, petrology, and cooling history of 14161,7373: A plutonic lunar sample with textural evidence of granitic-fraction separation by silicate-liquid immiscibility. American Mineralogist, 84, 821–837.

Jolliff, B.L., Wiseman, S.A., Lawrence, S.J., Tran, T.N., Robinson, M.S., Sato, H., Hawke, B.R., Scholten, F., Oberst, J., Hiesinger, H., and others. (2011) Non-mare silicic volcanism on the lunar farside at Compton-Belkovich. Nature Geoscience, 4, 566–571.

Kihara, K. (1978) Thermal change in unit-cell dimensions, and a hexagonal structure of tridymite. Zeitschrift für Kristallographie, 148, 237–253.

Klein, C. Jr., Drake, J.C., and Frondel, C. (1971) Mineralogical, petrological, and chemical features of four Apollo 12 lunar microgabbros. Proceedings of the 2nd Lunar Science Conference, 1, 265–284.

Korotev, R.L., Jolliff, B.L., Zeigler, R.A., Seddio, S.M., and Haskin, L.A. (2011) Apollo 12 revisited. Geochimica et Cosmochimica Acta, 75, 1540–1573.

Lakshtanov, D.L., Sinogeikin, S.V., and Bass, J.D. (2007) High-temperature phase transitions and elasticity of silica polymorphs. Physics and Chemistry of Minerals, 34, 11–22.

Lawrence, D.J., Elphic, R.C., Feldman, W.C., Prettyman, T.H., Gasnault, O., and Maurice, S. (2003) Small-area thorium features on the lunar surface. Journal of Geophysical Research, 108, 5102.

Ling, Z.C., Wang, A., and Jolliff, B.L. (2011) Mineralogy and geochemistry of four lunar soils by laser Raman study. Icarus, 211, 101–113. http://dx.doi.org/10.1016/j.icarus.2010.08.02.

Lucey, P., Korotev, R.L., Gillis, J.J., Taylor, L.A., Lawrence, D., Campbell, B.A., Elphic, R., Feldman, B., Hood, L.L., Hunten, D., and others. (2006) Understanding the lunar surface and space-Moon interactions. Reviews in Mineralogy and Geochemistry, 60, 83–219.

Marvin, U.B., Lindstrom, M.M., Holmberg, B.B., and Martinez, R.R. (1991) New observations on the quartz monzodiorite-granite suite. Proceedings of Lunar and Planetary Science Conference, 21, 119–135.

McMillan, P.F., Wolf, G.H., and Lambert, P. (1992) A Raman-spectroscopic study of shocked single crystalline quartz. Physics and Chemistry of Minerals, 19, 71–79.

Neal, C.R., Hacker, M.D., Snyder, G.A., Taylor, L.A., Liu, Y.-G., and Schmitt, R.A. (1994) Basalt generation at the Apollo 12 site, part 1: New data, classification, and re-evaluation. Meteoritics, 28, 334–338.

Ohtani, E., Ozawa, S., Miyahara, M., Ito, Y., Mikouchi, T., Kimura, M., Sato, K., and Hiraga, K. (2011) Coesite and stishovite in a shocked lunar meteorite, Asuka-881757, and impact events in lunar surface. Proceedings of the National Academy of Sciences, 108, 463–466.

Papike, J.J., and Cameron, M. (1976) Crystal chemistry of silicate minerals of geophysical interest. Reviews of Geophysics and Space Physics, 14, 37–80.

Papike, J.J., Spilde, M.N., Adcock, C.T., Fowler, G.W., and Shearer, C.K. (1997) Trace element fractionation by impact-induced volatilization: SIMS study of lunar HASP samples. American Mineralogist, 82, 630–634.

Quick, J.E., James, O.B., and Albee, A.L. (1981) Petrology and petrogenesis of lunar breccia 12013. Proceedings of Lunar and Planetary Science Conference, 12, 117–172.

Robinson, K.L., and Taylor, G.J. (2011) Intrusive and extrusive lunar felsites. Lunar and Planetary Science Conference XLII, Abstract 1257.

Ryder, G. (1976) Lunar sample 15405: Remnant of a KREEP basalt-granite differentiated pluton. Earth and Planetary Science Letters, 29, 255–268.

Rykart, R. (1995) Quarz-Monographie: Die Eigenheiten von Bergkristall, Rauchquarz, Amethyst, Chalcedon, Achat, Opal und anderen Varietäten. Thun-Ott Verlag, 2nd ed.

Schmahl, W.W., Swainson, I.P., Dove, M.T., and Graeme-Barber, A. (1992) Landau free energy and order parameter behaviour of the α/β phase transition in cristobalite. Zeitschrift für Kristallographie, 201, 125–145.

Seddio, S.M., Jolliff, B.L., Korotev, R.L., and Zeigler, R.A. (2013) Petrology and geochemistry of lunar granite 12032,366-319 and implications for lunar granite petrogenesis. American Mineralogist, 98, 1697–1713.

Seddio, S.M., Jolliff, B.L., Korotev, R.L., and Carpenter, P.K. (2014) Thorite in an Apollo 12 granite fragment and age determination using the electron microprobe. Geochimica et Cosmochimica Acta, 135, 307–320.

Sippel, R.F. (1971) Luminescence petrography of the Apollo 12 rocks and comparative features in terrestrial rocks and meteorites. Proceedings of the 2nd Lunar Science Conference, 1, 247–263.

Sippel, R.F., and Spencer, A.B. (1970) Luminescence petrography and properties of lunar crystalline rocks and breccias. Proceedings of the Apollo 11 Lunar Science Conference, 1, 2413–2426.

Smith, J.V., and Steele, I.M. (1976) Lunar mineralogy: a heavenly detective story. Part II. American Mineralogist, 61, 1059–1116.

——— (1984) Chemical substitution in silica polymorphs. Neues Jahrbuch für Mineralogie Monatshefte, 3, 137–144.

Smith, J.V., Anderson, A.T., Newton, R.C., Olsen, E.J., and Wyllie, P.J. (1970) Petrologic history of the moon inferred from petrography, mineralogy and petrogenesis of Apollo 11 rocks. Proceedings of the Apollo 11 Lunar Science Conference, 1, 897–925.

Stewart, D.B., Ross, M., Morgan, B.A., Appleman, D.E., Huebner, J.S., and Commeau, R.F. (1972) Mineralogy and Petrology of Lunar Anorthosite 15415. Abstracts of the 3rd Lunar Science Conference, 726.

Wang, A., Korotev, R.L., Jolliff, B.L., and Ling, Z.C. (2014) Raman imaging of extraterrestrial materials. Planetary and Space Science, in press, http://dx.doi.org/10.1016/j.pss.2014.10.005.

Wark, D.A., and Watson, E.B. (2006) TitaniQ: a titanium-in-quartz geothermometer. Contributions to Mineralogy and Petrology, 152, 743–754.

Warren, P.H., Taylor, G.J., Keil, K., Shirley, D.N., and Wasson, J.T. (1983) Petrology and chemistry of two 'large' granite clasts from the moon. Earth and Planetary Science Letters, 64, 175–185.

Wenk, H-.R., and Bulakh, A. (2003) Minerals: Their Constitution and Origin, Cambridge University Press, U.K.

Will, G., Bellotto, M., Parrish, W., and Hart, M. (1988) Crystal structures of quartz and magnesium germanate by profile analysis of synchrotron-radiation high-resolution powder data. Journal of Applied Crystallography, 21, 182–191.

MANUSCRIPT RECEIVED MAY 14, 2014
MANUSCRIPT ACCEPTED DECEMBER 30, 2014
MANUSCRIPT HANDLED BY STEVE SIMON